Acta Materialia 215 (2021) 117051

Contents lists available at ScienceDirect

Acta Materialia

journal homepage: www.elsevier.com/locate/actamat

Carbon stoichiometry and mechanical properties of high entropy carbides

M.D. Hossain[a,*], T. Borman[a], A. Kumar[b], X. Chen[b], A. Khosravani[c], S.R. Kalidindi[c], E.A. Paisley[d], M. Esters[e], C. Oses[e], C. Toher[e], S. Curtarolo[e], J.M. LeBeau[b], D. Brenner[f], J-P Maria[a]

[a] Department of Materials Science and Engineering, The Pennsylvania State University, University Park, PA 16802, USA
[b] Department of Materials Science and Engineering, Massachusetts Institute of Technology, Cambridge, MA 02139, USA
[c] Woodruff School of Mechanical Engineering, Georgia Institute of Technology, Atlanta, GA 30332, USA
[d] Sandia National Laboratories, Albuquerque, New Mexico 87123, USA
[e] Center for Autonomous Materials Design and Department of Mechanical Engineering and Materials Science, Duke University, Durham, NC 27708, USA
[f] Department of Materials Science and Engineering, North Carolina State University, Raleigh, NC 27695, USA

ARTICLE INFO

Article history:
Received 8 September 2020
Revised 4 May 2021
Accepted 1 June 2021
Available online 8 June 2021

Keywords:
High entropy carbide
Carbon stoichiometry
Nano-indentation
Mechanical property
Hardness
First principle calculation

ABSTRACT

The search for new materials via compositional exploration has recently led to the discovery of entropy stabilized and high entropy ceramics. The chemical diversity in the cation sublattice of high entropy ceramics has led to many enhanced properties and applications such as reversible energy storage, low temperature water splitting, amorphous-like thermal transport in crystalline solids and enhanced mechanical properties. This work describes the synthesis and mechanical properties of high entropy (HfNbTaTiZr)C_x thin films as a function of carbon content. The nature of the bonding and microstructure evolves as the material transforms from metallic to ceramic to nanocomposite with variations in the quantity and types of carbon, yielding large variations in the film hardness. Through multiple characterization techniques and first principles investigations, we separate the roles of microstructure and bonding characteristics in the mechanical property development of (HfNbTaTiZr)C_x thin films. This study presents a strategy to establish the bonding, structure, and property relationships in chemically disordered high entropy ceramics, largely based on the relative populations of filled or empty antibonding states for which there are new abilities to do so in high configurational entropy systems that exhibit high solubility of diverse cations while retaining rocksalt structure.

1.0. Introduction

Ultra high temperature ceramics (UHTCs) are often defined as ceramic materials with melting points in excess of 3000 °C [1]. The selection of UHTCs is dominated by elements from groups IVB and VB in carbide, nitride and diboride forms [2–7]. High performance UHTCs are critical for applications in extreme environments, such as heat shields of hypersonic vehicles, engines and components in nuclear reactors [4]. In addition to high melting temperatures, this class of materials exhibits high hardness, thermal conductivity, and chemical resistance [8,9]. The Extreme demands of the envisioned applications necessitate consideration of the strength, thermal expansion, and thermal conductivity of UHTCs across a wide range of temperatures. Furthermore, the UHTC must also satisfy the manufacturability, cost, and density requirements of the application at hand [1,4]. Consequently, there has been a renewed focus on the development of UHTC materials with tailored combinations of physical, mechanical, and chemical properties in order to enable these new applications. In the recent past, the development of new materials via compositional exploration has been dominated by the concept of high entropy alloys (HEAs) [10,11]. These new materials typically contain five distinct metals in a solid solution exhibiting FCC or BCC structure, with configurational entropy favoring the formation of a single phase over the precipitation of intermetallics: the number of species is beyond the threshold of the unavoidable disorder promotion [12]. The concept of HEAs was extended to ceramics with the first entropy stabilized oxide synthesized by Rost et al. [13].

Since then, the field of high entropy ceramics has grown to include UHTCs, such as high entropy diborides (HEBs), high entropy carbides (HECs), and high entropy nitrides (HENs), with numer-

* Corresponding author.
E-mail address: mzh606@psu.edu (M.D. Hossain).

https://doi.org/10.1016/j.actamat.2021.117051
1359-6454/

ous favorable findings [14–22]. Gild et al. demonstrated that HEBs possess enhanced mechanical and chemical properties relative to any of the binary constituents [14]. Castle et al. reported that bulk quinary carbides exhibited enhanced hardness compared to both binary and ternary counterparts [15]. High entropy carbides were observed to have improved oxidation, irradiation resistance and thermal stability [17,23–25]. Malinovskis et al. reported that physical vapor deposited (CrNbTaTiW)C_x films exhibited increased hardness and corrosion resistance [26]. The hardnesses of bulk spark plasma sintered HECs were reported to exceed the rule of mixtures by Sarker et al. [19]. Finally, Rost et al. reported atypical thermal conductivity evolution in (HfZrTaMoW)C_x as a function of carbon stoichiometry [27].

The diverse functional properties of transition metal carbides result from the combination of covalent, ionic, and metallic bonding characteristics. However, the presence of carbon vacancies in the binary carbides can have profound effects on both the melting temperature and the mechanical properties [3,28]. A computational study of the Hf-Ta-C system by Hong et al. found that the entropy from a carbon vacancy concentration between 10-20% had a positive effect on the energetic stability of binary and ternary carbides, thereby increasing the melting point [3]. Carbon vacancy induced hardening has also been reported in transition metal nitrides and carbides, increasing the hardness through a variety of mechanisms [29–31].

High entropy carbides show promise as a means to develop UHTC materials with a unique combination of properties including enhanced oxidation and chemical resistance, high melting temperature, and improved mechanical properties relative to their binary constituents [15,18,19,27]. The strong impact of carbon vacancies on the properties of binary and ternary carbides necessitates a complimentary study using a chemically disordered HEC. This work describes how types (bonded vs excess) and the amount of carbon affect mechanical properties and microstructure of a prototypical sputter deposited HEC, (HfNbTaTiZr)C_x. (HfNbTaTiZr)C was chosen based on the likelihood of forming a single-phase solid solution. As all the binary constituents of this composition are thermodynamically stable in the rock salt structure, the high entropy composition is expected to form a chemically disordered rock salt carbide. In addition, the binary constituents of this carbide are found to possess exceptional mechanical and physical properties – for example, HfC_x, TaC_x and (HfTa)C_x demonstrated melting temperatures > 4000 K [3]. A distinguishing feature of this work, particularly for high configurational entropy systems, is the focus on accurate carbon content characterization and systematic explorations of structure and property over a deliberate spectrum of metal-to-carbon ratios. Additionally, the experimental mechanical property findings are validated through ab-initio investigations.

2.0. Experimental methods

2.1. Thin film synthesis

Thin films were deposited with reactive radio frequency (RF) magnetron sputtering in a high vacuum chamber. A 99.5% HfNbTaTiZr alloy target (2" diameter) containing an equimolar fraction of each transition metal was sputtered at 200 W to provide the metal flux. Carbon was introduced in the form of 99.99% CH_4 gas, where the flow rate was used to control the total carbon content of the films. The carbide films were deposited on epi-polished *c*-plane sapphire substrates at a temperature of 650 °C, using a rotating substrate stage to ensure uniformity. Ultra-high purity (99.999%) argon was introduced to the chamber at a constant rate of 20 sccm, while the total pressure during deposition was fixed at 5 mTorr. Deposition rates were calibrated to determine the time necessary to achieve an approximate thickness of 2 microns, with actual thicknesses measured *ex situ* post-deposition. Before each deposition, the target was presputtered for 5 min in argon to clean the surface, followed by 2 min in the mixed Ar + CH_4 flow to allow pressure equilibration. A 2-micron film required roughly 90 min of deposition.

2.2. X-ray diffraction (XRD)

X-ray diffraction patterns of films were collected with a Panalytical Empyrean X-ray diffractometer using Cu Kα radiation (operating at 45 kV / 40 mA). The incident beam was shaped by a Bragg-Brentano HD optic with a 4 mm mask, 0.04 rad soller slits, and 1/8- and 1/2-degree divergence and anti-scatter slits, respectively. The diffracted beam passed through a ¼ degree anti-scatter slit and 0.04 rad soller slits before being collected by a PIXcel-3D detector operating in 1D scanning line mode. The data were collected with a count time of 75 s per 0.0263-degree 2θ step.

2.3. Scanning electron microscopy (SEM)

Field-emission scanning electron microscopy was used to analyze the surface and cross-sectional microstructures of the samples. Micrographs were collected with the in-lens detector of a Zeiss Sigma VP-FESEM, using a beam energy of 5 keV and a working distance of 3 mm. Cross sections were sputter coated with 5 nm of iridium to ground the insulating sapphire, preventing image drift. Film thicknesses were measured from multiple cross-sectional images across the sample.

2.4. X-ray photoelectron spectroscopy (XPS)

The types of carbon (bonded vs excess) in the film and their relative amounts were determined from X-ray photoelectron spectra collected with a Physical Electronics VersaProbe II. A monochromatic Al Kα X-ray source with an energy of 1486.6 eV was used to generate the photoelectrons for measurement. The spectra were measured with a hemispherical analyzer (pass energy of 58.7 eV) and analyzed with the CasaXPS 2.3.19 software package. Data were fit with modified Lorentzian line shape (LF) and Shirley background. All samples were presputtered for 5 min with a 3keV Ar^+ beam to remove any adventitious C and native oxide from the surface. High resolution XPS spectra were collected for the C 1*s*, Hf 4*f*, Ta 4*f*, Zr 3*d*, Nb 3*d*, and Ti 2*p* shells in order to avoid peak overlaps.

2.5. Scanning transmission electron microscopy (STEM)

Thin film carbide samples were characterized using STEM. Cross-section TEM samples were prepared by mechanical polishing with further thinning using Ar-ion milling from 2 kV to 0.1 kV. STEM imaging, energy-dispersive X-ray spectroscopy (EDS) and electron energy loss spectroscopy (EELS) were performed with a probe-corrected FEI Titan G2 60–300kV operated at 200kV with a beam current of 80 pA and probe convergence semi-angle of 19.6 mrad. Four-dimensional (4D) STEM was performed in microprobe mode with a beam current of 80 pA and a probe convergence semi-angle of 4.1 mrad. 4D STEM datasets were collected with an Electron Microscope Pixel Array Detector (EMPAD) [32]. Drift and scan-coil distortion correction has been applied to the atomically resolved bright-field (BF) images using RevSTEM [33].

2.6. Nanoindentation

Mechanical properties of the films were measured using a Hysitron TI-900 nanoindenter with a load resolution of 1 nN. A Berkovich indenter with a maximum applied load of 5.5 mN was used to produce the indents. Loading and unloading cycles were

set to 5 s each with a 2 s hold at the maximum load. Nine indents were measured on each sample, and the Oliver-Pharr method [34,35] was employed to calculate the hardness and modulus of the films. A polycarbonate sample was used to calibrate the tip to optic distance, and a fused silica specimen was used to determine the tip area function. The elastic moduli of the samples were calculated using the following relationship:

$$\frac{1}{E_r} = \frac{1-\upsilon_i^2}{E_i} + \frac{1-\upsilon_s^2}{E_s} \tag{1}$$

where E_r is the reduced elastic modulus, ν_i and E_i are the Poisson's ratio and elastic modulus of the diamond indenter, and ν_s and E_s are the Poisson's ratio and elastic modulus of the sample. The Poisson's ratios of the samples (ν_s) were determined from DFT calculations.

Another set of nanoindentation tests were collected using a spherical indenter tip on an Agilent G200 nanoindenter system with an XP head equipped with a continuous stiffness measurement (CSM). The spherical indentation stress-strain analysis protocols have been demonstrated in a variety of materials over a range of different material structure length scales [36–40]. In contrast to the hardness protocols, the spherical indentation stress-strain analysis results show low sensitivity to the sample surface quality, the indenter tip geometry and size, and indentation load/depth. The protocol consists of two main steps. The first step involves establishing an effective initial contact (i.e., zero-point) of the indenter contact with the sample surface. The second step uses the continuous stiffness measurement and elastic analyses using Hertz's theory to estimate the contact radius in the entire elastic-plastic loading segment. The estimated contact radius is then used to calculate the indentation stress and indentation strain at any point in the loading history applied to the sample. Details of the analysis can be found in the supplementary documents. The result of this protocol is an indentation stress-strain curve that typically exhibits a clear linear elastic regime followed by a smooth transition to the elastic-plastic regime. An indentation yield strength is estimated using a 0.2% plastic indentation strain offset.

2.7. Computational methods

The first principles calculations used the generalized gradient approximation (GGA) method implemented in Quantum Espresso v6.2 [41]. An 80 atom supercell based on rocksalt parent structure was populated with transition metal atoms (Hf, Nb, Ta, Ti, Zr) based on experimental compositions. The Alloy Theoretic Automated Toolkit (ATAT) software package [42] was used to distribute transition metals across cation sites in a special quasirandom structure (SQS). Anion sites were occupied by randomly distributed carbon atoms and carbon vacancies. A 3x3x3 k-point grid based on Monkhorst-Pack scheme was used for energy calculation, and an 8x8x8 k-point grid was used for electronic structure generation. The plane wave energy cutoff was set to 120 Ry and convergence with respect to the energy cutoff and k-points was confirmed. Norm-conserving non-relativistic pseudopotentials under Perdew–Burke-Ernzerhof (PBE) exchange-correlation functionals were used for all of the elements [43].

Bulk moduli were calculated using the Murnaghan equation of state by curve fitting the energy vs. volume data (total 15 data points). Elastic moduli were calculated by distorting the structure using $\boldsymbol{R}'=(1+\boldsymbol{\epsilon})\boldsymbol{R}$ in conjunction with the strain tensors found below. The variables $\boldsymbol{R}$ and $\boldsymbol{R}'$ are the original and distorted lattice vectors, respectively. In all cases, the total distortion of the structure was kept to less than 1%. [44–46].

$$\varepsilon_{tetr} = \frac{1}{3}\begin{pmatrix} -\delta & 0 & 0 \\ 0 & -\delta & 0 \\ 0 & 0 & 2\delta \end{pmatrix} \tag{2}$$

$$\varepsilon_{orth} = \frac{1}{3}\begin{pmatrix} 0 & \delta & 0 \\ \delta & 0 & 0 \\ 0 & 0 & \delta^2 \end{pmatrix} \tag{3}$$

The three independent elastic constants of the cubic system (C_{11}, C_{12}, and C_{44}) were calculated from the energy-strain relationships of the distorted cells and the bulk modulus using the following equations:

$$U_{tetr} = \frac{1}{3}(C_{11} - C_{12})\delta^2 \tag{4}$$

$$U_{orth} = 2C_{44}\delta^2 \tag{5}$$

$$B = \frac{1}{3}(C_{11} + 2C_{12}) \tag{6}$$

Although disorder breaks the symmtery calculations assuming a cubic symmetry have shown to predict the elastic tensors fairly accurately [47]. The resulting elastic constants and bulk modulus (listed in Table S3) were used to calculate the theoretical hardness with the model developed by Chen et al. [48] Eq. (7) defines the hardness as a function of the Pugh's modulus ratio (k) and the shear modulus (G). The Pugh's modulus ratio is in turn a function of the shear and bulk moduli, as shown in Eq. (8). The shear modulus was calculated from the three independent elastic moduli using Eq. (9) [44–46].

$$H_v = 2(k^2G)^{0.585} - 3 \tag{7}$$

$$k = \frac{G}{B} \tag{8}$$

$$G = \frac{3(C_{11} - C_{12}) + C_{44}}{5} \tag{9}$$

3.0. Results and discussion

Our initial experiment determined the relationship between metal flux/methane flow ratio and phase evolution. To do so, a sample series across the accessible ratio spectrum was fabricated and evaluated by a combination of XRD, XPS, and SEM. Out of plane X-ray diffraction scans for a film set prepared under constant metal flux and temperature, but with methane flow rates from 0.5 sccm to 5.5 sccm are presented in Fig. 1. Over this range, one observes a transformation from metallic, to carbide, to carbide/carbon composite states. Throughout the manuscript data are categorized into low (0.5–2.75 sccm), intermediate (2.8–3.5 sccm), and high (4.5–5.5 sccm) methane flow rates as these produce three different film types. At low methane flows ~0.5 sccm we produce a polycrystalline mixture of BCC and HCP metallic structures; as more methane is added, the film rapidly transforms into a carbon-deficient rock salt carbide with polycrystalline texture and broad diffraction peaks. At ~2.8 sccm, the film grows epitaxially with <111> rock salt || [0001] sapphire. In-plane azimuthal scans confirm in-plane registry with two populations of grains rotated by 60° with respect to each other. Above 3.5 sccm, the rocksalt carbide reverts to polycrystalline texture, producing broader diffraction peaks with diminished intensity. With the exception of the 0.5 sccm flow rate, which exhibits mixed metallic structures, all samples exhibit the rock salt structure exclusively. Even in this carbon-starved state, the large configurational entropy and structural/chemical similarity of the binary constituents favors a solid solution over phase segregation or intermetallic formation.

Given the broad compositional flexibility known to metal carbides, it is important to quantify carbon occupancy across this processing space. As a function of increasing methane flow rate, the

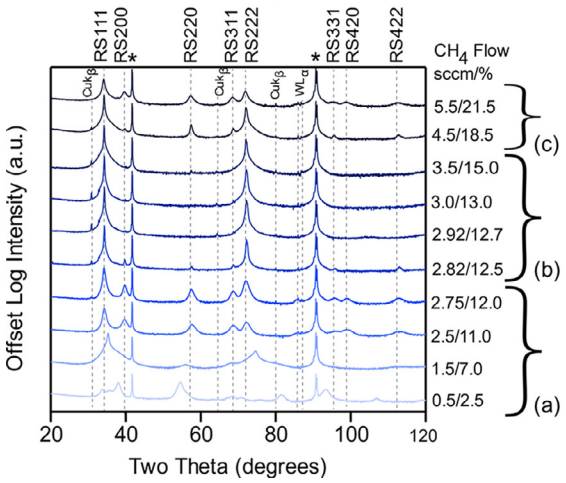

Fig. 1. X-ray diffraction (XRD) patterns from (HfNbTaTiZr)C_x high entropy carbide (HEC) films deposited at a range of methane flows. The patterns are categorized based on the structural development of the HEC: (a) low flow regime 0.5–2.75 sccm CH_4, XRD peaks correspond to polycrystalline metallic (~0.5 sccm) and rock salt carbide (1.5–2.75 sccm) (b) intermediate flow rates 2.82–3.5 sccm CH_4, epitaxial growth mode, and (c) high flow rate 4.5–5.5 sccm, poly crystalline growth mode, RS denotes rock salt structure peaks and * represents the sapphire substrate peaks. The CH_4 flow rate in sccm and percent of gas flow into the chamber are indicated on the right.

phase evolution induced by the gradual carbon increase can be explained by two distinct carbon populations: C can occupy the rock salt anion lattice sites forming C-metal bonds, or it can precipitate and form C-C bonds [9,49,50]. X-ray photoelectron spectroscopy (XPS) measurements explored both possibilities. High resolution XPS spectra of the C 1*s* and Ta 4*f* peaks are plotted with the corresponding curve fits in Fig. 2 for the entire methane flow series.

Low methane flow rate samples show a single C 1*s* peak at ~282.5 eV, except for a high energy shoulder at ~284.8 eV in the 2.75 sccm sample (Fig. 2a): the former represents the carbon-metal bonds whose intensity increases with methane flow rate; the latter indicates C-C bonds, and presumably a saturated carbide lattice with an excess carbon second phase. In the intermediate regime the excess carbon peak increases with methane flow while the C-metal bond intensity remains constant (Fig. 2b). The amount of bonded carbon affects the relative peak positions of the metals. As an example, Fig. 2(d–f) shows the Ta 4*f* peak evolution with methane flow. The Ta binding energy gradually increases (as shown by the $4f_{7/2}$ and $4f_{5/2}$ peaks) indicating an increasing concentration of carbon-metal bonds (Fig. 2d). The peak positions and intensities saturate at 2.75 sccm, coincident with an emerging excess-carbon shoulder. The metal peak intensities are essentially constant in the intermediate and high methane flow rates indicating Ta-C bonds saturation.

Transition metal carbides and high entropy carbides are stable under extreme substoichiometry: the rocksalt structure can tolerate 50% carbon vacancies, which substantially alters the properties [26,51]. For the present series, bonded and total (bonded + excess) carbon contents are plotted in Fig. 2g (normalized by metal atoms). Both quantities vary substantially. At a 2.75 sccm flow rate, the ratio of carbon to metal is nearly unity. This value accounts for preferential sputtering in XPS as discussed in the supplementary information.

In a high entropy carbide lattice, a random distribution of five different cations would lead to a configurational entropy equivalent to ~1.61R from the cation sublattice. However, based on the methane flow rate as anion vacancies are created, there will be an additional entropic contribution from the anion sublattice, assuming the rocksalt structure remains intact. As demonstrated in Fig. 1a, the rocksalt structure could be stabilized with up to ~50% or more C vacancies in the structure. Consequently, a high entropy composition, such as $(Hf_{0.2}Nb_{0.2}Ta_{0.2}Ti_{0.2}Zr_{0.2})C_{0.5}$, acquires a large configurational entropy of ~2.30R that includes both sublattice contributions and assumes vacancies are randomly distributed. The low enthalpic penalty associated with carbon vacancy formation and the subsequent entropic contribution to the free energy enable such a high percentages of carbon vacancies without structural disintegration [3]. Frequently, highly carbon-deficient deposition conditions – a low methane flow rate – would encourage an enthalpy-driven metal rich Ta_2C ($P\bar{3}m1$), Nb_2C ($P6_3/mmc$), $TiC_{0.59}$

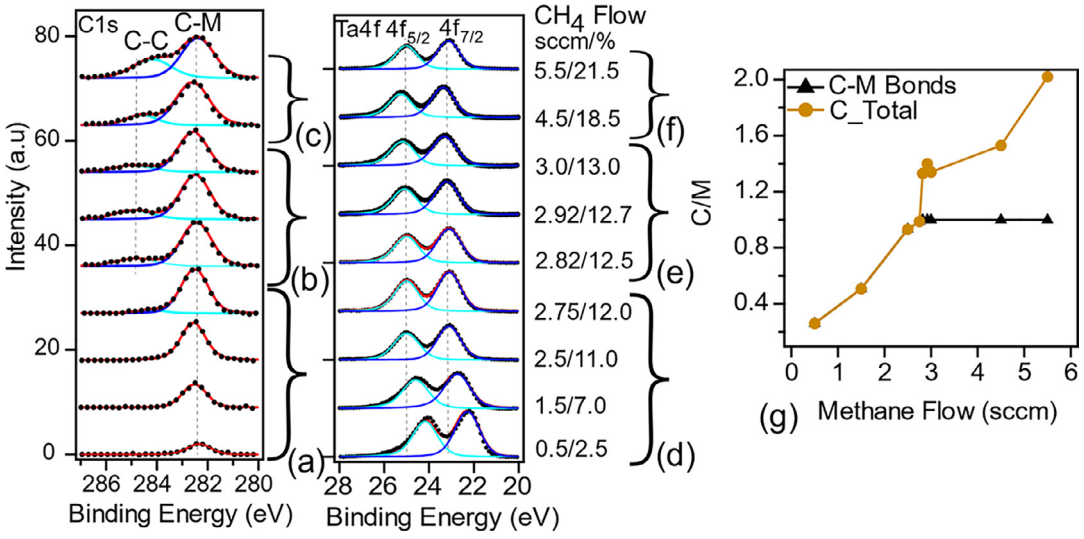

Fig. 2. High resolution XPS data of C 1*s* and Ta 4*f* peaks and resulting analysis. The C 1*s* peak (a) low flow rate: only C-M bond (carbon bonded to metal) present except a weak shoulder for 2.75 sccm where the C-C bond (excess carbon) peak is incipient (b) intermediate flow rate: fully developed C-C bonded peaks are observed. (c) high flow rate: both C peaks are present, the relative contribution from C-C bonded peak increases with flow rate. For Ta 4*f* peak (d) low flow rate: systematic shift in the Ta $4f_{7/2}$ and $4f_{5/2}$ observed as the structure transforms from metallic to rock salt carbide (e),(f) intermediate and high flow rate respectively: both peak positions are fixed throughout last two flow regime. (g) Carbon to metal (C/M) ratios are plotted as a function of methane flow rate. The number of C-M bonds increases with flow rate, the deviation between the total carbon and carbon bonded to metal leads to the precipitation of the excess carbon after 2.75 sccm which is the point of saturation.

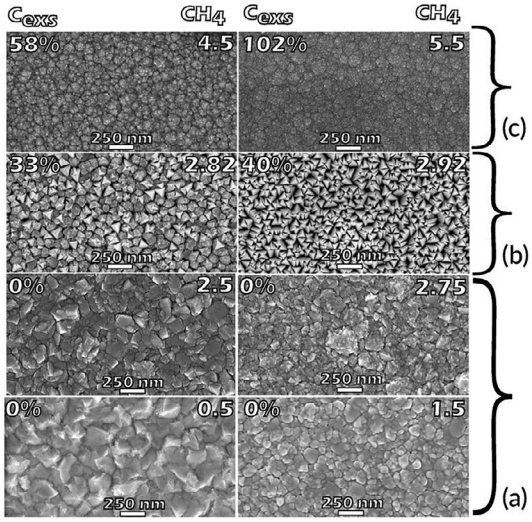

Fig. 3. Microstructural evolution of thin films as a function of increasing methane flow rate, (a) low flow rate samples: microstructure changes from a large metallic grain towards rock salt carbide with different grain morphology from equiaxed to irregular shape (b) intermediate flow rate- morphology of the grain changes to triangular shape with precipitation of large amount of excess carbon (c) high flow rate-finally triangular grain morphology transforms to equiaxed nanocrystalline grains. The flow rates are designated in sccm, the excess carbon (C_{exs}) in each flow rate are also shown.

($R\bar{3}mH$) phase evolution. It is unclear whether the chemical disorder in the cation sublattice substantially impacts the ultimate phase evolution, preserves the carbon-deficient rocksalt phase, and prevents any metal rich phase development. An investigation to understand this phenomenon is currently in progress. However, higher methane flows produce excess carbon precipitation, which interestingly is accompanied by improvements in crystallinity and texture.

Excess carbon is thus associated with a two phase microstructure and a transition to epitaxial growth. SEM imaging reveals a pronounced change in surface morphology and grain size as shown in Fig. 3. Large metallic grains (200±20 nm) are observed at 0.5 sccm flow rate. With increasing methane flow from 1.5–2.75 sccm (Fig. 3a) grain size decreases and becomes less regular. In the intermediate flow regime (2.8–3.5 sccm), more than 30% excess carbon precipitates and is accompanied by a transition to epitaxial growth and a regular triangular grain morphology (Fig. 3b). The triangular grains assemble in two domains reflecting the 3-fold symmetry of the underlying c-plane sapphire ($R\bar{3}c$) substrate. The lattice mismatch between rock salt {111} high entropy carbide and c-sapphire is approximately 14% [18,19]. However, the manner in which excess carbon promotes epitaxy is not currently understood. Epitaxial columnar growth is also verified from the cross-sectional scanning electron micrograph as presented in the supplementary information in Fig. S4.

Further increases in the methane flow (4.5–5.5 sccm CH_4) suppress columnar growth and produce a very fine-grained nanocomposite microstructure (Fig. 3c). In this flow regime greater than 50% excess carbon precipitation appears to restrict carbide grain growth and provides numerous nucleation sites, resulting in nanocrystalline carbide grains. Similar microstructural features have been observed in sputter deposited binary carbides, where researchers concluded- excess carbon regulates the carbide grain size and grain separation [9,52,53]. If one approximates the nanocrystalline grains as columnar rectangular prisms separated by excess carbon, for 3 sccm and 5.5 sccm nanocomposite films, average grain separations are ~4.0 nm and ~1.2 nm respectively (calculation details in SI and Fig. S5). Hence, the bonded and excess carbon quantity regulates bonding characteristics, microstructure evolution, and subsequently functional properties of high entropy carbide films.

Scanning transmission electron microscopy (STEM) allows us to probe microstructure, chemistry, and phase at the nanometer length scale using various imaging and spectroscopic techniques. Here, samples deposited under low (2.5 sccm) and intermediate (3 sccm) methane flow rates were selected for STEM investigation. Fig. 4a shows a low-angle annular dark field (LAADF) STEM image from the 2.5 sccm sample revealing the presence of structural defects in carbon deficient samples. Higher magnification bright-field (BF) STEM images show that these are {111} type planar defects, specifically stacking faults and twin boundaries as shown in Fig. 4b. In contrast, the intermediate flow rate 3 sccm sample is free of such planar defects (Fig 4c and d).

The thin film chemical uniformity has been examined using energy dispersive spectroscopy (EDS) in STEM mode. Metallic elements are found to be uniformly distributed across the film for both samples as shown in Fig. 4 e and f that represents 2.5 and 3 sccm samples respectively; however, slight striation from titanium at the grain boundaries are evident.

The grain boundaries were further investigated with STEM electron energy loss spectroscopy (EELS). The EELS elemental maps in Fig. 4g and h, in combination with EDS (Fig. 4 e, f) indicate carbon, oxygen, and titanium are enriched in the grain boundaries. The low flow rate 2.5 sccm sample grain boundary is crystalline, as shown in the accompanying atomic resolution micrograph in Fig. 4g. Conversely, the intermediate flow rate 3 sccm sample grain boundary appears poorly crystalline (Fig. 4h). In order to examine the crystallinity, diffraction patterns were collected from the 3 sccm sample grain and grain boundaries using 4D STEM (Fig. S6). The carbide grains diffract strongly and generate a diffraction pattern consistent with the {111} oriented epitaxial growth. In contrast, diffuse scattering from the grain boundaries confirms amorphous or poorly crystalline characteristics. EELS spectra of Carbon *K* edge at the grain boundary is also found to resemble amorphous carbon as shown in Fig. S7.

Among the constituent metallic elements of $(HfNbTaTiZr)C_x$ high entropy carbide, titanium is the smallest and lightest, as well as oxidation prone. These factors likely promoted titanium segregation in the grain boundaries during deposition at 650 °C. Although titanium, oxygen, and carbon were detected in the grain boundary region via STEM EELS and EDS, there were no indications that any crystalline titanium oxides or oxycarbides had formed. This suggests that the deposition temperature and stoichiometry (particularly the intermediate flow rate 3 sccm case) were insufficient to crystallize any Ti-C-O phases [54].

Raman spectroscopy is a widely used tool to characterize the sp^2 and sp^3 bonded carbon in thin films. The poorly crystalline excess carbon in $(HfNbTaTiZr)C_x$ films were further explored by Raman spectroscopy (Fig. S8) to confirm the bonding characteristics of the carbon. The low flow rate samples (0.5–2.75 sccm) Raman spectra are flat and featureless in the region of interest (800–2000 cm^{-1}). Samples deposited at or above 2.82 sccm show broad peaks which correspond to the D (1350 cm^{-1}, defect induced breathing mode) and G (1580 cm^{-1}, sp^2 bonding) modes of carbon. The carbon Raman peaks materialize at an identical flow rate when excess carbon precipitates as measured by XPS (Fig. 2). The excess carbon at grain boundary shows characteristics (D and G peak position, peak intensities) similar to the diamond-like carbon phase formation. The XPS, TEM, and Raman data conclusively establish that the excess carbon precipitates at the grain boundaries which are poorly crystalline in nature. Thus, methane flow rates during deposition regulates the microstructure and phase evolution, controls the metal carbon bonding, and consequently tailors the physical properties.

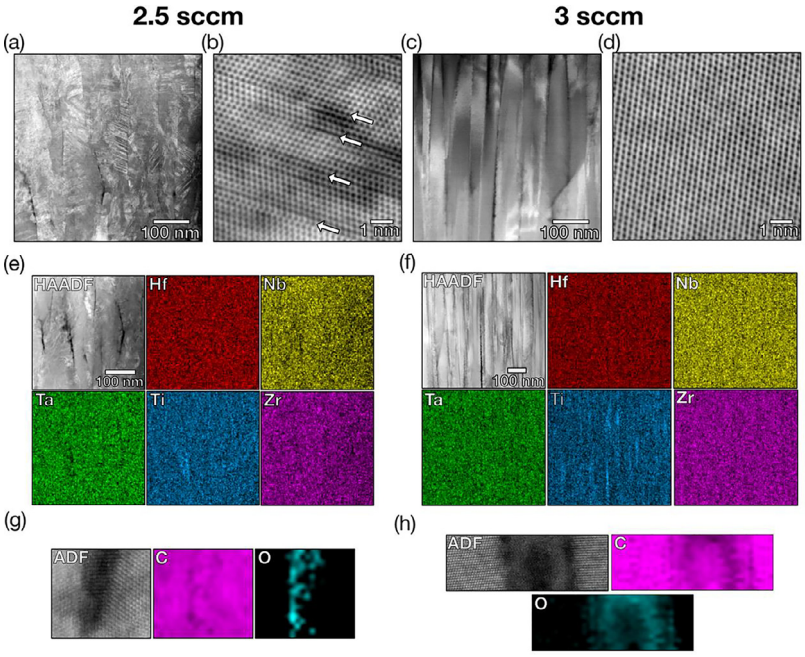

Fig. 4. STEM analysis of a low flow rate- 2.5 sccm and intermediate flow rate- 3 sccm high entropy carbide samples. Low flow rate 2.5 sccm sample: (a) low angle annular dark field image (LAADF) reveals defects in the microstructure (b) high resolution bright-field (BF) STEM image show planar defects in the crystal. The intermediate flow rate 3 sccm sample: (c) LAADF and (d) high resolution BF STEM indicates elimination of defects, (e) high angle annular dark field image (HAADF) STEM image and energy dispersive spectroscopy (EDS) map of 2.5 sccms sample, (f) HAADF STEM image and EDS map of 3 sccm sample, (g) annular dark field (ADF) STEM image and electron energy loss spectroscopy (EELS) elemental map of a grain boundary for low flow rate 2.5 sccm film and (h) similar analysis of a grain boundary for intermediate flow rate 3 sccm film.

To establish the microstructure, bonding and property relationship, film hardness for all flow rates were measured by nanoindentation, while density functional theory was used to calculate hardness for supercells reflecting the experimentally determined compositions. Both values are plotted as a function of increasing methane flow rate in Fig. 5a. At low flow rates (0.5–2.75 sccm), the experimental hardness increases linearly with increasing methane flow, reaching a maximum value of 24 ± 3 GPa at 2.75 sccm. The hardness drops to 10 ± 1.5 GPa at intermediate flow rates (2.82-3.5 sccm) and persists through the entire spectrum. At high flow rates (4.5–5.5 sccm) hardness rises to ~15 ± 1 GPa.

At low methane flow rates (0.5–2.75 sccm) carbon occupies the anion lattice sites in the rock salt structure, where it engages in strong covalent bonds (see Fig. 6). The hardness increases linearly with carbon-metal bond density and the maximum hardness coincides with anion lattice saturation at 2.75 sccm flow rate. At intermediate flow rates (2.82–3.5 sccm), the measured hardness drops sharply due to carbon precipitation between carbide grains (Fig. 5a). The poorly crystalline excess carbon at grain boundaries likely promotes sliding movement between the grains thus eroding the mechanical response (Figs. 4 g, h and S8).

At high flow rates (4.5–5.5 sccm) the nanocomposite microstructure evolves and the hardness recovers. This behavior can be explained as the combination of three distinct strengthening effects: grain size reduction, nanocomposite formation, and strengthening from the sp^3 bonding in the diamond-like carbon phase. As described in the SEM analysis (Fig. 3c), the transition from intermediate to high methane flow rates is accompanied by a microstructural transformation from large triangular grains to a nanocrystalline carbide. The excess carbon in the grain boundary likely restricts grain growth and fosters nanocrystalline carbide grains [9,52].

As discussed previously the excess carbon interface is four times thinner in a nanocomposite microstructure compared to the epitaxial films and the nanocrystalline carbide grains are better connected to each other due to the thin interface. Also, the grains are polycrystalline in nature at this high methane flow rate as evident from the XRD and SEM analysis. The combination of a thin interface and random grain orientation changes the fracture behavior compared to the textured columnar grains.

Finally, the diamond-like carbon (DLC) phase formation is evident from the Raman spectroscopy analysis (Fig. S8) [55]. The high flow rate (4.5–5.5 sccm) depositions are associated with greater than 50% excess carbon precipitation, ergo, the DLC matrix dominates the mechanical behavior. The DLC phase hardness varies between 10-20 GPa [56–58]. The nanocomposite film hardness values lie in the range estimated by rule of mixing predictions for stoichiometric high entropy carbides and a DLC phase. The sp^3 bonding in the DLC phase strengthens the carbon matrix which likely mitigates mechanical failure associated with composite interfaces.

Ab-initio calculations provide an avenue to validate the given explanations for the mechanical property trends by decoupling the bonding and microstructural effects. As it is impractical to simulate a multiphase microstructure through first principles calculations, only the carbon deficient and stoichiometric single-phase high entropy compositions were simulated by density functional theory (DFT). Analogous to the experimental data, the DFT calculations predict that hardness increases linearly as a function of carbon content or methane flow rate in the experiment (Fig. 5a). For the stoichiometric and close-to-stoichiometric carbides calculated and measured hardness agree well. For highly deficient compositions, calculations underpredict hardness. We speculate that this discrepancy originated in part from the random SQS supercells which do not capture the carbon vacancy clustering that is pervasive in the TEM analysis. More precise and computationally intensive methods considering segregation [59] and partial order [60] in disordered mixtures could describe this clustering and its effect on hardness, and they are planned for the future.

However, the calculated and measured hardness of the extremely carbon deficient samples also deviate due to the limita-

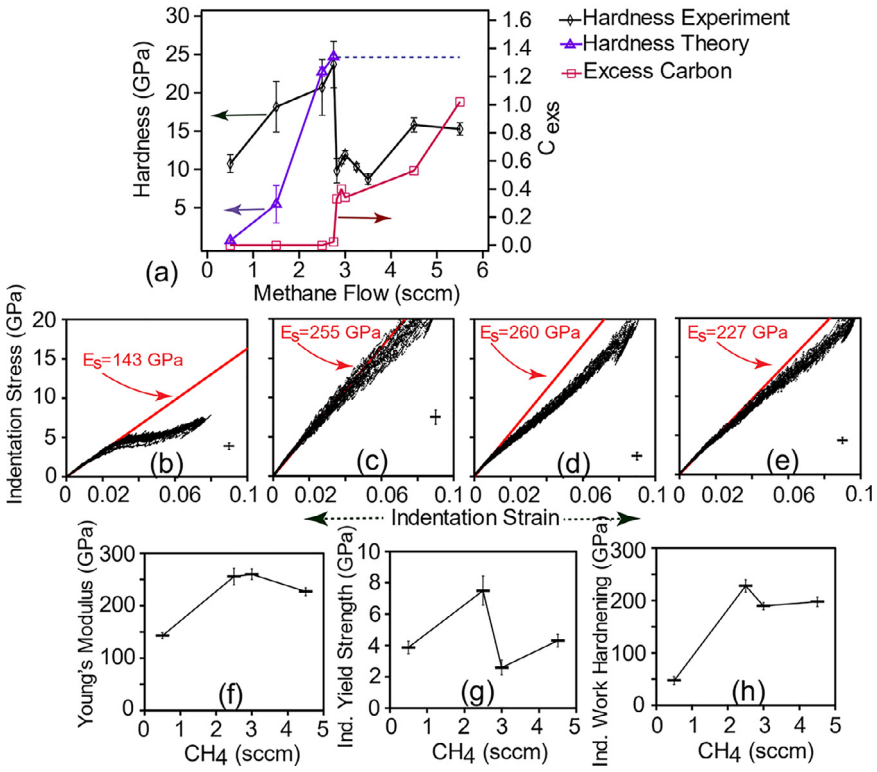

Fig. 5. (a) Experimental and theoretical hardness as a function of methane flow rate, experimental data: low flow rate (0.5–2.75 sccm) hardness increases linearly; intermediate flow rate (2.82–3.5 sccm), hardness drops abruptly and stays steady; high flow rate (4.5–5.5 sccm), hardness ascended to a higher value. Theoretical data: DFT calculated hardness of low flow rate samples increases up to point of saturation of anion sublattice which are protracted to show the stoichiometric carbides contribution to the intermediate and high flow rates. Indentation stress-strain curves obtained by using a spherical indenter are presented for (b and c) low flow rate 0.5 and 2.5 sccm; (d) intermediate flow rate 3 sccm; (e) high flow rate 4.5 sccm samples. (f–h) Extracted Young's modulus, Indentation yield strength, and indentation work hardening extracted from the curves.

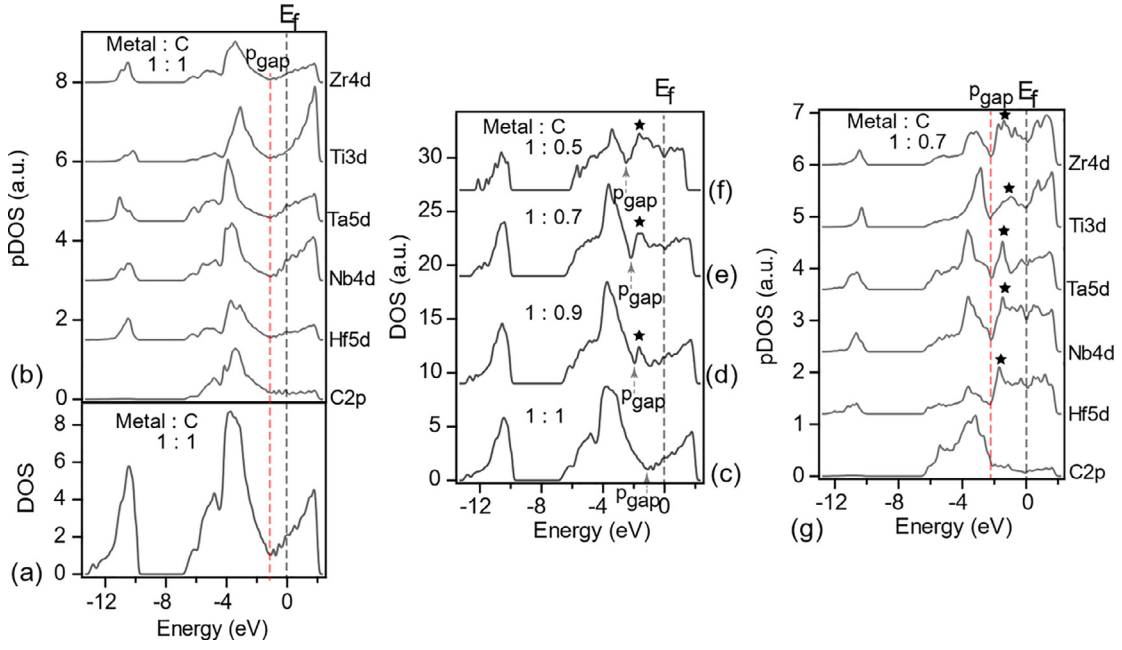

Fig. 6. The electronic structure evolution of low flow rate high entropy carbide samples, the selected compositions are based on the XPS analyzed compositions as a function of CH_4 flow rate during deposition (a) electronic structure of stoichiometric carbide with metal:C=1:1 corresponds to the composition of 2.75 sccm CH_4 flow rate, (b) pDOS of stoichiometric high entropy carbide showing C 2*p*, Hf 5*d*, Nb 4*d*, Ti 3*d*, Zr 4*d* contribution; electronic structure of (c) stoichiometric composition- replotted to show the pseudogap position; (d) composition with flow rate of 2.5 sccm CH_4 with metal:C=1:0.9, (e) an intermediate structure with 30% C vacancy metal:C=1:0.7 (f) composition with flow rate of 1.5 sccm CH_4 with metal:C=1:0.5 (g) pDOS of high entropy carbide structure with 30% C vacancy showing C 2*p*, Hf 5*d*, Nb 4*d*, Ti 3*d*, Zr 4*d* contribution. p_{gap} indicates the pseudogap region, ★ represents the new energy states generated due to C vacancy, vertical grey dotted line is the Fermi level (E_F) and red dotted line is the pseudogap (p_{gap}). (For interpretation of the references to color in this figure legend, the reader is referred to the web version of this article.)

tions of the protocol followed to calculate theoretical hardness. Theoretical hardness was calculated based on the elastic constants of the material, more specifically the shear and bulk moduli (see experimental Section 2.7 calculation method). The hardness of covalently bonded materials is dictated by the covalent bond strength, which is directly related to the elastic constants of the material. Hence, predictions are accurate for stoichiometric or nearly stoichiometric compositions where the high density of strong covalent bonds controls the plastic deformation process. Conversely, for extreme-carbon-deficient samples, the fraction of metallic bonding will increase, in which case the mechanical properties depend increasingly on plastic flow, dislocation formation, glide, and interactions with defects (dislocations, vacancies, grain boundaries, etc.). As the present calculations do not capture these phenomena, one anticipates a discrepancy in measured vs. calculated hardness. In addition, since the DFT calculations were performed for single phase rock-salt carbides, we infer that the sudden drop in experimental hardness above 2.75 sccm methane flow is due to excess carbon precipitation and microstructural modifications.

The transition of our carbide samples from a carbon-deficient metallically bonded crystal to a stoichiometric covalent carbide was explored mechanically by recording the stress-strain response under a spherical indenter as shown in Fig. 5(b)–(e). These figures show indentation stress-strain curves using a 16μm tip radius on samples with CH_4 flow rates of 0.5, 2.5, 3, and 4.5 sccm, respectively. In each sample 20 indentation stress-strain curves were collected. The highlighted red band shows the extracted values of indentation yield strength within one standard deviation from the average. The extracted Young's modulus, the indentation yield strength, and the indentation work hardening rates are presented in Fig. 5 (f)–(h). The response from the 0.5 sccm sample stress-strain curve is different from other samples. This sample quickly becomes non-linear due to yielding and plastic deformation, a typical response from a metallic crystal. In comparison, curves for other samples show very high hardening rate due to a different nature of atomic bonding, smaller grain size, and the presence of twin boundaries in some samples. The effect of twinning on indentation yield strength is obvious between samples with flow rate of 2.5 and 3 sccm. As presented in Fig. 4(a) and 4(b), the microstructure of the 2.5 sccm sample consists of numerous nanotwins while the microstructure of the 3 sccm sample is almost defect free (Fig. 4c,d), and therefore a higher indentation yield strength and a higher indentation work hardening rate is expected.

The dependence of bonding on carbon content was further investigated by evaluating the electronic structures of stoichiometric and carbon deficient crystals using DFT. The carbon stoichiometries were selected based on the XPS data, with metal to carbon ratios 1:1, 1:0.9, and 1:0.5 coinciding with low flow rates 2.75, 2.5, and 1.5 sccm CH_4 samples, respectively. Additionally, an intermediate composition with a metal to carbon ratio 1:0.7 was added, this stoichiometry is expected for 2 sccm flow of methane during deposition.

The stoichiometric high entropy carbide ($Hf_{0.2}Nb_{0.2}Ta_{0.2}Ti_{0.2}Zr_{0.2}$)C electronic structure is shown in Fig. 6a. The minima in the electronic structure represents the pseudogap (p_{gap}). Energy states below the pseudogap are bonding in nature whereas states above pseudogap exhibit antibonding characteristics. The Fermi level is located above the pseudogap indicating a fraction of occupied antibonding states that are typically metallic in nature [61–63]. To identify the constituents that contribute bonding and antibonding electrons a partial density of states (pDOS) analysis was completed. Fig. 6(b) shows the individual contributions. The carbon 2*p* orbital and metal *d* orbitals contribute strongly to the energy states below the pseudogap, with a peak at -3 eV. The metal *d* and carbon *p* orbital overlap are a signature of covalent bonding that leads to high hardness in the stoichiometric film. In contrast, the majority of antibonding states are associated with metal *d* orbitals, and thus a signature of metallicity if populated.

Similar calculations were performed as a function of carbon deficiency. Fig. 6(d)–(f) show the total density of states for 10, 30, and 50% vacant carbon sites. With decreasing carbon concentration, we observe a shift in the pseudogap to lower energies and an increasing population of new antibonding states above it – these new states are indicated by the star inset.

Again, a partial density of states analysis was performed in order to determine which orbitals contributed to these new states, the results are shown in Fig. 6(g) corresponding to the 30% carbon deficient case. The energy distribution of states from carbon 2*p* orbitals remains largely unchanged, while it is clear the new states that emerge above p_{gap} are clearly associated with metal *d* orbitals. Populating these new states above p_{gap} produce a less intense and narrower *p-d* hybridized pseudo-valence band (around -3 eV as shown in Fig. S9) which, in comparison to the stoichiometric case, signifies fewer covalent bonds. This reduction lowers the hardness as one replaces covalently bonded metal electrons with new metallic states. In the present DFT calculation scheme, carbon vacancies are randomly distributed in a rock salt structure. As such, it does not reflect the possibility of vacancy ordering in a chemically disordered crystal or its consequences for the mechanical properties.

Medvedeva et al. studied the electronic structure of binary WC_x and TaC_x with 12.5% C vacancies and they also found that anion vacancies introduce new states surrounding the Fermi level [64]. Such DFT calculations provide an opportunity to track electronic structure evolution with carbon content, and understand the origins of property dependencies. Furthermore, in these high entropy systems where solubility of diverse cations is possible, one can use this learning to predict how valence electron concentration will shift by formulation (provided the rock salt structure is sustained) and in turn how the mechanical properties will respond.

However, in this study, the stoichiometric (HfNbTaTiZr)C measured hardness is lower compared to previous reports [15,19,65]. As demonstrated from SEM micrograph analysis, present rf sputtering deposition conditions resulted in carbides with grain sizes of 100–200 nm. The bulk ceramic processing methods regularly produce high entropy carbides with grain sizes of 10–50 μm and nanoindentation hardness $>$ 30 GPa [15,19]. Wang et al. showed that the Vickers hardness of high entropy carbides substantially decreased from ~16 to ~9 GPa when the grain size decreased from 16 μm to 400 nm [66]. Therefore, we attribute the observed reduced hardness compared to bulk samples to the grain size softening effect, but further studies are required in this domain.

Furthermore, carbon vacancies greatly affect the mechanical properties of binary and ternary transition metal carbides and nitrides, where a certain percentage of sub-stoichiometry, i.e. ~12.5% C vacancy, could optimize the mechanical response [28–30]. This phenomenon-vacancy induced hardening and its underlying mechanism – has been explained based on electronic band filling [29] and changes in microstructural features [28] due to vacancy clustering that prompted pronounced resistance to dislocation flow in the crystal. We are unable to determine whether carbon vacancies give rise to similar hardening effects in high entropy carbides due to the coarse selection in methane flow rates that produced crystals with 75% (~0.5 sccm), 50% (~1.5 sccm), 7% (~2.5 sccm), and 0% (~2.75 sccm) C vacancies. Present first principles calculations predict crystal softening with increasing carbon vacancy. Our analysis agrees with previous studies that illustrated carbon vacancy effects on elastic and plastic properties of binary carbides [28]. Hence, the observed hardness trend is determined to be the effect of bonding rather than any microstructural feature or vacancy induced hardening effects. At this point, further studies are

required that involve the synthesis of high entropy carbides with close control over carbon vacancy evolution combined with micro and macroscale mechanical properties investigations.

4.0. Conclusions

The study focused on the synthesis and properties of the high entropy carbide, $(HfNbTaTiZr)C_x$, as a function of carbon stoichiometry. Thin films were synthesized over a broad range of carbon stoichiometries using reactive RF magnetron sputtering. The resulting films exhibited structural transitions from metallic, to carbide, and finally carbide-carbon nanocomposite structures, simply by changing the methane flow during the deposition. The highest hardness of 24 ± 3 GPa was obtained from a stoichiometric $(Hf_{0.2}Nb_{0.2}Ta_{0.2}Ti_{0.2}Zr_{0.2})C$ film. Ab-initio calculations revealed that the hardness of stoichiometric films is dictated by the covalent bond density, with microstructure playing a negligible role. The anion vacancies in the high entropy crystal introduces new occupied metallic states that inadequately compensate for the lost strong covalent bonds, resulting in a reduced hardness for samples synthesized at lower than stoichiometric flow rate. However, a modest increase in methane flow above the stoichiometric flow rate, lowered the hardness to ~10 ± 1.5 GPa due to the formation of a two phase microstructure. The poorly crystalline excess carbon precipitation weakened the grain boundaries of the epitaxial carbide film, facilitating easy fracture. High resolution imaging revealed, despite the chemically disordered metal sublattice, that anion vacancies clustered in stacking faults similar to the Group VB carbides. Overall, carbon substoichiometry appears to have similar effects on the bonding, microstructure, and properties of high entropy carbides and binary carbides.

Declaration of Competing Interest

The authors declare that they have no known competing financial interests or personal relationships that could have appeared to influence the work reported in this paper.

Acknowledgement

This research is funded by the U.S. Office of Naval Research Multidisciplinary University Research Initiative (MURI) program under Grant No. N00014-15-1-2863. The computational part supported by the TACC-XSEDE allocation projects TG-DMR180016 and TG-DMR170083. TB acknowledges the funding from National Science Foundation Graduate Research Fellowship- Grant No. DGE-1255832. Authors acknowledge Materials Characterization Laboratory (MCL) at Pennsylvania State University for SEM and XPS characterization and Analytical Instrumentation Facility (AIF) at North Carolina State University for TEM study, which was supported by the State of North Carolina and the NSF under Award No. ECCS-1542015. The AIF is a member of the North Carolina Research Triangle Nanotechnology Network (RTNN), a site in the National Nanotechnology Coordinated Infrastructure (NNCI). This work made use of instrumentation at AIF acquired with support from the NSF (No. DMR-1726294). Any opinions, findings, and conclusions or recommendations expressed in this material are those of the authors and do not necessarily reflect the views of the Office of Naval Research and the National Science Foundation.

Supplementary materials

Supplementary material associated with this article can be found, in the online version, at doi:10.1016/j.actamat.2021.117051.

References

[1] E. Wuchina, E. Opila, M. Opeka, W. Fahrenholtz, I. Talmy, UHTCs: ultra-high temperature ceramic materials for extreme environment aplications, Electrochem. Soc. Interface (2007) 30–36.
[2] O. Cedillos-Barraza, D. Manara, K. Boboridis, T. Watkins, S. Grasso, D.D. Jayaseelan, R.J.M. Konings, M.J. Reece, W.E. Lee, Investigating the highest melting temperature materials: a laser melting study of the TaC-HfC system, Sci. Rep. 6 (2016) 37962, doi:10.1038/srep37962.
[3] Q.J. Hong, A. Van De Walle, Prediction of the material with highest known melting point from ab initio molecular dynamics calculations, Phys. Rev. B Condens. Matter Mater. Phys. 92 (2015) 1–6, doi:10.1103/PhysRevB.92.020104.
[4] W.G. Fahrenholtz, E.J. Wuchina, W.E. Lee, Y. Zhou, Ultra-High Temperature Ceramics: Materials for Extreme Environment Applications, John Wiley & Sons, 2014, doi:10.1002/9781118700853.
[5] D.K. Deardorff, M.I. Copeland, R.P. Adams, The hafnium-carbon phase diagram, U.S. Dep. of the Interior Bureau of Mines, Washington, DC, 1967. https://www.tib.eu/en/search/id/TIBKAT%3A472391607/The-hafnium-carbon-phase-diagram/.
[6] R.A. Andrievskii, N.S. Strel'nikova, N.I. Poltoratskii, E.D. Kharkhardin, V.S. Smirnov, Melting point in systems ZrC-HfC, TaC-ZrC, TaC-HfC, Sov, Powder Metall. Met. Ceram. 6 (1967) 65–67, doi:10.1007/BF00773385.
[7] C. Oses, C. Toher, S. Curtarolo, High-entropy ceramics, Nat. Rev. Mater. 5 (2020) 295–309, doi:10.1038/s41578-019-0170-8.
[8] S. Wang, K. Zhang, T. An, C. Hu, Q. Meng, Y. Ma, M. Wen, W. Zheng, Structure, mechanical and tribological properties of HfCx films deposited by reactive magnetron sputtering, Appl. Surf. Sci. 327 (2015) 68–76, doi:10.1016/j.apsusc.2014.11.130.
[9] U. Jansson, E. Lewin, Sputter deposition of transition-metal carbide films-a critical review from a chemical perspective, Thin Solid Films 536 (2013) 1–24, doi:10.1016/j.tsf.2013.02.019.
[10] M.H. Tsai, J.W. Yeh, High-entropy alloys: a critical review, Mater. Res. Lett. 2 (2014) 107–123, doi:10.1080/21663831.2014.912690.
[11] D.B. Miracle, O.N. Senkov, A critical review of high entropy alloys and related concepts, Acta Mater. 122 (2017) 448–511, doi:10.1016/j.actamat.2016.08.081.
[12] C. Toher, C. Oses, D. Hicks, S. Curtarolo, Unavoidable disorder and entropy in multi-component systems, Npj Comput. Mater. 5 (2019), doi:10.1038/s41524-019-0206-z.
[13] C.M. Rost, E. Sachet, T. Borman, A. Moballegh, E.C. Dickey, D. Hou, J.L. Jones, S. Curtarolo, J.P. Maria, Entropy-stabilized oxides, Nat. Commun. 6 (2015) 8485, doi:10.1038/ncomms9485.
[14] J. Gild, Y. Zhang, T. Harrington, S. Jiang, T. Hu, M.C. Quinn, W.M. Mellor, N. Zhou, K. Vecchio, J. Luo, High-entropy metal diborides: a new class of high-entropy materials and a new type of ultrahigh temperature ceramics, Sci. Rep. 6 (2016) 2–11, doi:10.1038/srep37946.
[15] E. Castle, T. Csanádi, S. Grasso, J. Dusza, M. Reece, Processing and properties of high-entropy ultra-high temperature carbides, Sci. Rep. 8 (2018).
[16] V.F. Gorban, A.A. Andreyev, G.N. Kartmazov, A.M. Chikryzhov, M.V. Karpets, A.V. Dolomanov, A.A. Ostroverkh, E.V. Kantsyr, Production and mechanical properties of high-entropic carbide based on the TiZrHfVNbTa multicomponent alloy, J. Superhard Mater. 39 (2017) 166–171, doi:10.3103/S1063457617030030.
[17] J. Zhou, J. Zhang, F. Zhang, B. Niu, L. Lei, W. Wang, High-entropy carbide: a novel class of multicomponent ceramics, Ceram. Int. 44 (2018) 22014–22018, doi:10.1016/j.ceramint.2018.08.100.
[18] T.J. Harrington, J. Gild, P. Sarker, C. Toher, C.M. Rost, O.F. Dippo, C. McElfresh, K. Kaufmann, E. Marin, L. Borowski, P.E. Hopkins, J. Luo, S. Curtarolo, D.W. Brenner, K.S. Vecchio, Phase stability and mechanical properties of novel high entropy transition metal carbides, Acta Mater. 166 (2019) 271–280, doi:10.1016/j.actamat.2018.12.054.
[19] P. Sarker, T. Harrington, C. Toher, C. Oses, M. Samiee, J.-P. Maria, D.W. Brenner, K.S. Vecchio, S. Curtarolo, High-entropy high-hardness metal carbides discovered by entropy descriptors, Nat. Commun. (2018) 1–10, doi:10.1038/s41467-018-07160-7.
[20] J.L. Braun, C.M. Rost, M. Lim, A. Giri, D.H. Olson, G.N. Kotsonis, G. Stan, D.W. Brenner, J. Maria, P.E. Hopkins, Charge-induced disorder controls the thermal conductivity of entropy-stabilized oxides, 1805004 (2018) 1–8. 10.1002/adma.201805004.
[21] S. Zhai, J. Rojas, N. Ahlborg, K. Lim, M.F. Toney, H. Jin, C. Chueh, A. Majumdar, The use of poly-cation oxides to lower the temperature of two-step thermochemical water splitting, Energy Environ. Sci. 11 (2018) 2172–2178, doi:10.1039/c8ee00050f.
[22] A. Sarkar, L. Velasco, D. Wang, Q. Wang, G. Talasila, L. de Biasi, C. Kübel, T. Brezesinski, S.S. Bhattacharya, H. Hahn, B. Breitung, High entropy oxides for reversible energy storage, Nat. Commun. 9 (2018) 3400, doi:10.1038/s41467-018-05774-5.
[23] B. Ye, T. Wen, Y. Chu, High-temperature oxidation behavior of $(Hf_{0.2}Zr_{0.2}Ta_{0.2}Nb_{0.2}Ti_{0.2})C$ high-entropy ceramics in air, J. Am. Ceram. Soc. 103 (2020) 500–507, doi:10.1111/jace.16725.
[24] Y. Tan, C. Chen, S. Li, X. Han, J. Xue, T. Liu, X. Zhou, H. Zhang, Oxidation behaviours of high-entropy transition metal carbides in 1200 °C water vapor, J. Alloy. Compd. 816 (2020) 152523, doi:10.1016/j.jallcom.2019.152523.
[25] F. Wang, X. Yan, T. Wang, Y. Wu, L. Shao, M. Nastasi, Y. Lu, B. Cui, Irradiation damage in $(Zr_{0.25}Ta_{0.25}Nb_{0.25}Ti_{0.25})C$ high-entropy carbide ceramics, Acta Mater. 195 (2020) 739–749, doi:10.1016/j.actamat.2020.06.011.
[26] P. Malinovskis, S. Fritze, L. Riekehr, L. von Fieandt, J. Cedervall, D. Rehnlund, L. Nyholm, E. Lewin, U. Jansson, Synthesis and characterization of multicom-

ponent (CrNbTaTiW)C films for increased hardness and corrosion resistance, Mater. Des. 149 (2018) 51–62, doi:10.1016/j.matdes.2018.03.068.
[27] C.M. Rost, T. Borman, M.D. Hossain, M. Lim, K.F. Quiambao-Tomko, J.A. Tomko, D.W. Brenner, J.P. Maria, P.E. Hopkins, Electron and phonon thermal conductivity in high entropy carbides with variable carbon content, Acta Mater. 196 (2020) 231–239, doi:10.1016/j.actamat.2020.06.005.
[28] X.X. Yu, G.B. Thompson, C.R. Weinberger, Influence of carbon vacancy formation on the elastic constants and hardening mechanisms in transition metal carbides, J. Eur. Ceram. Soc. 35 (2015) 95–103, doi:10.1016/j.jeurceramsoc.2014.08.021.
[29] S.H. Jhi, S.G. Louie, M.L. Cohen, J. Ihm, Vacancy hardening and softening in transition metal carbides and nitrides, Phys. Rev. Lett. 86 (2001) 3348–3351, doi:10.1103/PhysRevLett.86.3348.
[30] H. Holleck, Material selection for hard coatings, J. Vac. Sci. Technol. A Vac. Surf. Film 4 (1986) 2661–2669, doi:10.1116/1.573700.
[31] S.H. Jhi, J. Ihm, S.G. Loule, M.L. Cohen, Electronic mechanism of hardness enhancement in transition-metal carbonitrides, Nature 399 (1999) 132–134, doi:10.1038/20148.
[32] M.W. Tate, P. Purohit, D. Chamberlain, K.X. Nguyen, R. Hovden, C.S. Chang, P. Deb, E. Turgut, J.T. Heron, D.G. Schlom, D.C. Ralph, G.D. Fuchs, K.S. Shanks, H.T. Philipp, D.A. Muller, S.M. Gruner, High dynamic range pixel array detector for scanning transmission electron microscopy, Microsc. Microanal. 22 (2016) 237–249, doi:10.1017/S1431927615015664.
[33] X. Sang, J.M. LeBeau, Revolving scanning transmission electron microscopy: correcting sample drift distortion without prior knowledge, Ultramicroscopy 138 (2014) 28–35, doi:10.1016/j.ultramic.2013.12.004.
[34] G.M. Pharr, W.C. Oliver, Measurement of thin film mechanical properties using nanoindentation, MRS Bull. 17 (1992) 28–33, doi:10.1557/S0883769400041634.
[35] W.C. Oliver, G.M. Pharr, An improved technique for determining hardness and elastic modulus using load and displacement sensing indentation experiments, J. Mater. Res. 7 (1992) 1564–1583, doi:10.1557/jmr.1992.1564.
[36] S. Pathak, J.S. Weaver, C. Sun, Y. Wang, S.R. Kalidindi, N.A. Mara, Spherical Nanoindentation Stress-Strain Analysis of Ion-Irradiated Tungsten, Springer International Publishing, Cham, 2019, doi:10.1007/978-3-030-04639-2_40.
[37] J.S. Weaver, M.W. Priddy, D.L. McDowell, S.R. Kalidindi, On capturing the grain-scale elastic and plastic anisotropy of alpha-Ti with spherical nanoindentation and electron back-scattered diffraction, Acta Mater. 117 (2016) 23–34, doi:10.1016/j.actamat.2016.06.053.
[38] A. Khosravani, L. Morsdorf, C.C. Tasan, S.R. Kalidindi, Multiresolution mechanical characterization of hierarchical materials: Spherical nanoindentation on martensitic Fe-Ni-C steels, Acta Mater. 153 (2018) 257–269, doi:10.1016/j.actamat.2018.04.063.
[39] J.S. Weaver, V. Livescu, N.A. Mara, A comparison of adiabatic shear bands in wrought and additively manufactured 316L stainless steel using nanoindentation and electron backscatter diffraction, J. Mater. Sci. 55 (2020) 1738–1752, doi:10.1007/s10853-019-03994-8.
[40] A. Khosravani, C.M. Caliendo, S.R. Kalidindi, New insights into the microstructural changes during the processing of dual-phase steels from multiresolution spherical indentation stress-strain protocols, Metals 10 (2020) 23–29 (Basel), doi:10.3390/met10010018.
[41] P. Giannozzi, S. Baroni, N. Bonini, M. Calandra, R. Car, C. Cavazzoni, D. Ceresoli, G.L. Chiarotti, M. Cococcioni, I. Dabo, A. Dal Corso, S. De Gironcoli, S. Fabris, G. Fratesi, R. Gebauer, U. Gerstmann, C. Gougoussis, A. Kokalj, M. Lazzeri, L. Martin-Samos, N. Marzari, F. Mauri, R. Mazzarello, S. Paolini, A. Pasquarello, L. Paulatto, C. Sbraccia, S. Scandolo, G. Sclauzero, A.P. Seitsonen, A. Smogunov, P. Umari, R.M. Wentzcovitch, QUANTUM ESPRESSO: a modular and open-source software project for quantum simulations of materials, J. Phys. Condens. Matter. 21 (2009), doi:10.1088/0953-8984/21/39/395502.
[42] A. van de Walle, P. Tiwary, M. de Jong, D.L. Olmsted, M. Asta, A. Dick, D. Shin, Y. Wang, L.Q. Chen, Z.K. Liu, Efficient stochastic generation of special quasirandom structures, Calphad 42 (2013) 13–18, doi:10.1016/j.calphad.2013.06.006.
[43] J.P. Perdew, K. Burke, M. Ernzerhof, Generalized gradient approximation made simple, Phys. Rev. Lett. 77 (1996) 3865–3868, doi:10.1103/PhysRevLett.77.3865.
[44] Z. Wu, X.J. Chen, V.V. Struzhkin, R.E. Cohen, Trends in elasticity and electronic structure of transition-metal nitrides and carbides from first principles, Phys. Rev. B Condens. Matter Mater. Phys. 71 (2005) 1–5, doi:10.1103/PhysRevB.71.214103.
[45] D.G. Sangiovanni, V. Chirita, L. Hultman, Electronic mechanism for toughness enhancement in TixM$_{1-x}$N M=Mo and W), Phys. Rev. B Condens. Matter Mater. Phys. 81 (2010) 1–7, doi:10.1103/PhysRevB.81.104107.
[46] J. Yang, F. Gao, Hardness calculations of 5D transition metal monocarbides with tungsten carbide structure, Phys. Status Solidi Basic Res. 247 (2010) 2161–2167, doi:10.1002/pssb.201046127.
[47] F. Tasnádi, M. Odén, I.A. Abrikosov, Ab initio elastic tensor of cubic $Ti_{0.5}Al_{0.5}N$ alloys: dependence of elastic constants on size and shape of the supercell model and their convergence, Phys. Rev. B Condens. Matter Mater. Phys. 85 (2012) 1–9, doi:10.1103/PhysRevB.85.144112.
[48] X.Q. Chen, H. Niu, D. Li, Y. Li, Modeling hardness of polycrystalline materials and bulk metallic glasses, Intermetallics 19 (2011) 1275–1281, doi:10.1016/j.intermet.2011.03.026.
[49] E. Lewin, O. Wilhelmsson, U. Jansson, Nanocomposite nc-TiC/a-C thin films for electrical contact applications, J. Appl. Phys. (2006) 100, doi:10.1063/1.2336302.
[50] T. Zehnder, J. Patscheider, Nanocomposite TiC/a-C:H hard coatings deposited by reactive PVD, Surf. Coat. Technol. 133–134 (2000) 138–144, doi:10.1016/S0257-8972(00)00888-4.
[51] H.W. Hugosson, U. Jansson, B. Johansson, O.E. Eriksson, Phase stability diagrams of transition metal carbides, a theoretical study, Chem. Phys. Lett. 333 (2001) 444–450, doi:10.1016/S0009-2614(00)01414-7.
[52] T. Zehnder, P. Schwaller, F. Munnik, S. Mikhailov, J. Patscheider, Nanostructural and mechanical properties of nanocomposite nc-TiC/a-C:H films deposited by reactive unbalanced magnetron sputtering, J. Appl. Phys. 95 (2004) 4327–4334, doi:10.1063/1.1650898.
[53] M. Eizenberg, S.P. Murarka, Reactively sputtered titanium carbide thin films: preparation and properties, J. Appl. Phys. 54 (1983) 3190–3194, doi:10.1063/1.332478.
[54] R. K&ocirc, Y. Hashimoto, H. Kawasaki, Y. Yada, T. Tamura, M. Hirai, On the electrorefining of titanium from crude titanium containing carbon and oxygen, J. Jpn. Inst. Met. 35 (1971) 1055–1062, doi:10.2320/jinstmet1952.35.11_1055.
[55] A.C. Ferrari, Determination of bonding in diamond-like carbon by Raman spectroscopy, Diam. Relat. Mater. 11 (2002) 1053–1061, doi:10.1016/S0925-9635(01)00730-0.
[56] I. Hutchings, P. Shipway, Tribology, Friction and Wear of Engineering Materials, Second Edition2nd ed., Elsevier Ltd., 2017, doi:10.1016/S0007-8506(07)62632-8.
[57] J. Musil, P. Novák, R. Čerstvý, Z. Soukup, Tribological and mechanical properties of nanocrystalline-TiC/a-C nanocomposite thin films, J. Vac. Sci. Technol. A Vac. Surf. Film 28 (2010) 244–249, doi:10.1116/1.3294717.
[58] J. Robertson, Diamond-like amorphous carbon, Mater. Sci. Eng. R Rep. 37 (2002) 129–281, doi:10.1016/s0927-796x(02)00005-0.
[59] K. Yang, C. Oses, S. Curtarolo, Modeling off-stoichiometry materials with a high-throughput ab-initio approach, Chem. Mater. 28 (2016) 6484–6492, doi:10.1021/acs.chemmater.6b01449.
[60] Y. Lederer, C. Toher, K.S. Vecchio, S. Curtarolo, The search for high entropy alloys: a high-throughput ab-initio approach, Acta Mater. 159 (2018) 364–383, doi:10.1016/j.actamat.2018.07.042.
[61] J. Häglund, A. Fernndez Guillermet, G. Grimvall, M. Körling, Theory of bonding in transition-metal carbides and nitrides, Phys. Rev. B 48 (1993) 11685–11691, doi:10.1103/PhysRevB.48.11685.
[62] C.D. Gelatt, A.R. Williams, V.L. Moruzzi, Theory of bonding of transition-metals to non-transition metals, Phys. Rev. B 27 (1983) 2005–2013 ezaccess.libraries.psu.edu/10.1103/PhysRevB.27.2005.
[63] G.A. Fernández, J. Häglund, G. Grimvall, Cohesive properties of 4d-transition-metal carbides and nitrides in the NaCl-type structure, Phys. Rev. B 45 (1992) 11557–11567, doi:10.1103/PhysRevB.45.11557.
[64] N.I. Medvedeva, A.L. Ivanovskii, Effect of metal and carbon vacancies on the band structure of hexagonal tungsten carbide, Phys. Solid State 43 (2001) 469–472, doi:10.1134/1.1356121.
[65] B. Ye, T. Wen, M.C. Nguyen, L. Hao, C.Z. Wang, Y. Chu, First-principles study, fabrication and characterization of ($Zr_{0.25}$ $Nb_{0.25}$ $Ti_{0.25}$ $V_{0.25}$)C high-entropy ceramics, Acta Mater. 170 (2019) 15–23, doi:10.1016/j.actamat.2019.03.021.
[66] F. Wang, X. Zhang, X. Yan, Y. Lu, M. Nastasi, Y. Chen, B. Cui, The effect of submicron grain size on thermal stability and mechanical properties of high-entropy carbide ceramics, J. Am. Ceram. Soc. 103 (2020) 4463–4472, doi:10.1111/jace.17103.